Strain-Based Shape Reconstruction and Temperature Compensation for Fiber Bragg-Instrumented Rotor Blades

Tobias Pflumm
Technology & Innovation
Kopter Germany GmbH
Höhenkirchen-Siegertsbrunn, Germany

Andreas Jochum
Technology & Innovation
Kopter Germany GmbH
Höhenkirchen-Siegertsbrunn, Germany

Sören Süße
Technology & Innovation
Kopter Germany GmbH
Höhenkirchen-Siegertsbrunn, Germany

ABSTRACT

A pre-series Kopter AW09 main rotor blade was instrumented with fiber Bragg gratings (FBGs). Static lab tests supported by digital image correlation (DIC) were conducted to derive and evaluate mathematical relationships between the measured strain signals and structural quantities. These comprised the beam sectional strains, the elastic deformation of the blade, and the sectional loads and stiffness properties. Additionally, the paper addresses the challenge of isolating these target variables from the influence of temperature variations. In order to evaluate cross-sectional strains due to thermal influences, full-scale rotor test rig data recorded in non-rotating conditions was used as the basis for an in-field calibration, taking advantage of natural temperature changes. This accounted for the effect of temperature and its spatial gradients on the sectional signals of the anisotropic rotor blade.

NOTATION

AREA	Autonomous Rotorcraft for Extreme Altitudes
AW09	Kopter AW09 (single-engine helicopter)
AW139	Leonardo AW139 (twin-engine helicopter)
CAD	Computer aided design
CFD	Computational fluid dynamics
DIC	Digital image correlation
DFOSS	Direct fiber-optic shape sensing
DOF	Degree of freedom
EMC	Electromagnetic compatibility
FBG	Fiber Bragg grating
H135	Airbus Helicopters H135 (twin-engine helicopter)
HUMS	Health and usage monitoring system
iRoB	Instrumented rotor blade (BayLu25 project)
MERIT	Munich Experimental Rotor Investigation Testbed
R	Blade section (followed by radial distance in mm)
RMSE	Root mean square error
TUM	Technical University of Munich
c_{12}	Linear shear strain / twist rate coefficient
F	Cross-sectional stress resultant vector
K	Cross-sectional stiffness matrix
$\mathcal{K}$	Curvature tensor
k	Linear gauge factor
q	Quaternion
R	Rotation matrix
r	Displacement vector
s	Span-wise coordinate
S_1, S_2	Temperature probe calibration parameters
T	Temperature
W	Warping matrix under unit loads
x, y, z	Spatial coordinates
ε	Strain tensor
ε_c	Cross-sectional strain vector
$\bar{\varepsilon}_1$	Axial strain
ζ	Thermo-optical coefficient
θ_1	Ply / surface angle
κ_1	Twist rate
κ_2	Flap bending curvature
κ_3	Lead-lag bending curvature
λ	Bragg wavelength
Ψ_1	Warping function
$(.)_{ref}$	reference
$(.)_{mech}$	mechanical
$(.)_{ph}$	phantom
$(.)_{therm}$	thermal
$(.)_{SS}$	suction side
$(.)_{PS}$	pressure side

Presented at the 50th European Rotorcraft Forum, Marseille, France, Sept. 10–12, 2024.

INTRODUCTION

Traditionally, helicopter component lifespans are estimated based on loads that are encountered during design and qualification, with adjustments for known fleet issues. However, actual in-flight loads are rarely measured on production aircraft, leaving these predictions conservative and vulnerable to unforeseen circumstances. It has been accepted, that load monitoring on production aircraft has the potential to improve safety and to reduce maintenance costs. The adoption of this technology has been hindered by the limitations of traditional sensors and data acquisition systems, which are often bulky, heavy and unreliable in long-term use (Ref. 1).

Hajek, Manner and Süße (Refs. 2, 3) investigated the integration of fiber Bragg grating (FBG) sensors into the composite structure of an elastic H135 blade root. The authors concluded that the signal quality of the FBG sensors in terms of noise and linearity showed potential for future HUMS applications. Furthermore, the embedding of FBGs in a fiber composite structure promised robustness against environmental influences, EMC protection and good fatigue properties. Based upon the previous work, Süße (Ref. 4) refined an analysis method of strain measurements along the blade in order to determine the elastic deformation and bending stiffness of the AREA rotor blade (Ref. 5).

Building upon the concept of rotor-integrated health monitoring, Bottasso et al. (Ref. 6) presented for the Leonardo AW139 tail rotor a novel blade strain monitoring system, with which they demonstrated the feasibility of embedding FBG sensors directly into composite rotor blades. Furthermore, they showcased a complete interrogation system housed within a dedicated enclosure for harsh rotor hub environments.

Particular noteworthy is also the project BladeSense (Refs. 7–11), which utilized both fiber Bragg gratings for strain measurements and a direct fiber-optic shape sensing (DFOSS) approach based on differential interferometry for the recovery of deformation and the dynamic characterization of an H135 rotor blade. Beyond laboratory and test bench trials, the feasibility of the technology was evaluated through ground runs.

As part of the joint research project iRoB (*instrumented rotor blade*) of Kopter Germany and TUM, Berghammer et al. (Refs. 12, 13) assessed the impact of FBGs integrated into a composite rotor blade. They tested small samples with and without FBGs, and successfully embedded them into a small-scale blade for static and dynamic tests both in the lab and on the rotor test rig MERIT (Ref. 14).

The objective of this paper, created in the context of the research project iRoB, is to establish a mathematical relationship between the strain signals measured on a rotor blade and structural quantities such as beam sectional strains, the elastic deformation of the blade, and the sectional loads and stiffness properties. Additionally, the paper addresses the challenge of isolating these target variables from the influence of temperature variations.

INSTRUMENTATION

A pre-series AW09 main rotor blade was instrumented with FBGs in addition to electrical resistance strain gauges. Therefore, a total number of 60 FBG strain sensors was applied to five distinct sections at 820 mm (*R820*), 1505 mm (*R1505*), 2025 mm (*R2025*), 2795 mm (*R2795*) and 4470 mm (*R4470*) measured from the rotor rotation axis. The section at 3613 mm (*R3616*) was instrumented with two FBG temperature sensors, isolated in a stainless steel tube and spliced at the end of the fiber. One sensor was bonded to the suction side and one to the pressure side of the rotor blade. Each temperature probe was calibrated by the supplier with dedicated calibration parameters (T_{ref}, S_1, S_2, λ_{ref}). The strain sensors were bonded both in axial direction and in $\pm 45°$ pairs. Figure 1 shows an illustration of the sensor network and fiber routing. The unique sensor indexes refer to the fiber and grating numbers.

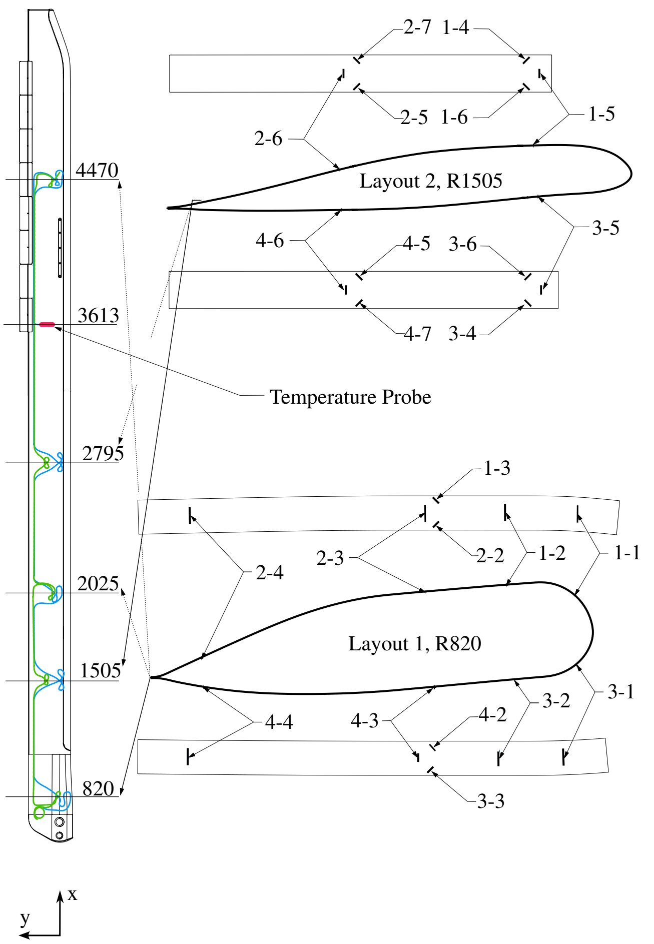

Figure 1. FBG sensor network and fiber routing on a pre-series AW09 rotor blade

The radial distribution was determined based on numerical modal analysis to capture at least the first five Eigenmodes of the rotor blade. The four optical fibers with their gratings were placed in the respective quadrants of the cross-section in such way, that under load the strains of each sensor of a fiber usually have equal signs. Sections R820, R2025 and R4470 had a layout that consisted of six axial strain sensors and two rosettes to maximize the bending signal-to-noise ratio. On the other hand, the layout selected for sections R1505 and R2795 contained four rosettes in order to capture the shear strain field in more detail. The fibers were bonded to the surface of the rotor blade in following steps: First, the surface was prepared for bonding by removing paint and primer until the structure was exposed. Then the sensor positions were measured and marked with dedicated stencils. The surface was cleaned from any contamination to ensure a good bond. Subsequently, the fiber was bonded with a fast curing adhesive under light pressure. Finally, the bonded surface was sealed and coated with transparent silicone to protect it from the environment and to allow inspection.

METHODOLOGY

The flowchart in Figure 2 illustrates the path from the measured signal quantities of the Bragg wavelengths via local strains and temperatures to cross-sectional strains, sectional forces as well as rotations and displacements of the rotor blade.

An interrogator induced a specified spectrum of light into each of the optical fibers. Each *strain sensor* and each *temperature sensor* reflected a wavelength specific to its Bragg grating back to the interrogator. The interrogator identified the peaks in the reflected optical spectrum and assigned the wavelength to the respective sensors. When a strain sensor experienced strain, the spacing between the repetitive structures within the Bragg grating altered, leading to a shift of the reflected wavelength. Such wavelength shift could also be the result of temperature fluctuations, which affected the refractive index of the fiber due to the thermo-optic effect. An approximated compensation of this effect was applied using the *local temperatures* at the two temperature probes, determined by Equation (2). The approximation assumed equal local temperatures at each surface point of a blade side. Subsequently, the *local strains* could be calculated with Equation (1) from the change of Bragg wavelength with the knowledge of the linear gauge factor $k = 7.6E^{-7}\ \mu\varepsilon^{(-1)}$, as well as the linear (ζ_1) and quadratic (ζ_2) components of the thermo-optical coefficient.

The main components of this study were based on the representation of the rotor blade as a beam and the determination of the *sectional strains* $\varepsilon_c = (\bar{\varepsilon}_1,\ \kappa_1,\ \kappa_2,\ \kappa_3)$, with the sectional axial strain $\bar{\varepsilon}_1$, the twisting rate κ_1, the flap bending curvature κ_2 and the lead-lag bending curvature κ_3. The transversal shear strains $\bar{\varepsilon}_2$ and $\bar{\varepsilon}_3$ were neglected for this analysis as they have an insignificant effect on the dynamic response of rotor blades. The relationship between measured strain signals and beam sectional strains is described in Equation (3) as linear kinematic strain-displacement relation and is derived and evaluated in Chapter KINEMATIC STRAIN-DISPLACEMENT RELATION.

Using an appropriate interpolation function between the five support cross-sections, the *rotations* and *displacements* of the rotor blade were integrated according to Equation (10), as described and validated in Chapter STRAIN-BASED SHAPE RECONSTRUCTION.

The sectional strains were also the basis of the TEMPERATURE COMPENSATION study, in which a relation according to Equation (4) between the temperature signals and the *thermal sectional strains* was derived from non-rotating tests on the rotor test rig. The model accounted for the anisotropic behavior of the rotor blade and allowed to determine the isolated *mechanical sectional strains*.

Finally, the sectional strains are related to the sectional loads to find the linear coefficients of the beam-sectional stiffness matrix according to Equation (6). The primary objective is to derive a relationship between the measured strain signals and sectional loads. The secondary objective is to evaluate the beam sectional stiffness matrices (K) to validate the structural numerical models of the rotor blade and the beam descriptions of aeromechanic models.

STATIC DEFORMATION MEASUREMENTS

Several static tests were carried out on a blade test rig in order to derive the kinematic strain-displacement relationship, validate the shape reconstruction and subsequently evaluate the stiffness matrices. The deformation field of the rotor blade under different load conditions was determined using digital image correlation.

The experimental setup is shown in Figure 3a. Two digital cameras were placed in a stereo configuration to perform 3D measurements. The surface structure of the rotor blade and the test rig were recognized based on attached point markers, which allowed to assign 3D coordinates to image pixels by triangulation. During the deformation of the specimen, images were taken and subsequently compared to the undeformed state in order to calculate the displacement and deformation of the object.

The rotor blade was mounted on the rotor calibration test rig and oriented in a position with the trailing-edge pointing upwards. A six degree-of-freedom (DOF) load cell was installed between two flanges at the attachment. The main blade reference coordinate system, as visualized in Figure 1 and Figure 3a, was oriented with the x-axis along the span of the rotor blade, the y-axis pointing towards the trailing-edge and the z-axis upwards. A random pattern of optical markers was distributed on the suction side surface of the rotor blade, on the blade clamp and on the cylindrical flanges. Additional LED arrays provided a homogeneous illumination of the test article. The used camera system was a *GOM ARAMIS SRX 1600* with lenses of 20 mm focal length. Prior to the measurements, it was necessary to ensure that the sensors had attained thermal equilibrium and to carry out a recalibration. The system allowed to capture images for full-field and point-based measurements with a resulting calibrated field of view of 4500 mm width and an image size of 4096x3068 pixels. With this setup an accuracy of the 3D coordinates for each optical marker of approximately 0.1 mm in-plane and 0.3 mm out-of-plane could be achieved.

Loads were applied using weights, which acted on a load frame via a cable pulley. Various load cases were recorded. For the purpose of evaluating deflections, the twist rate and the performance of the shape reconstruction algorithms, loads were applied to the direction of only one coordinate axis at a

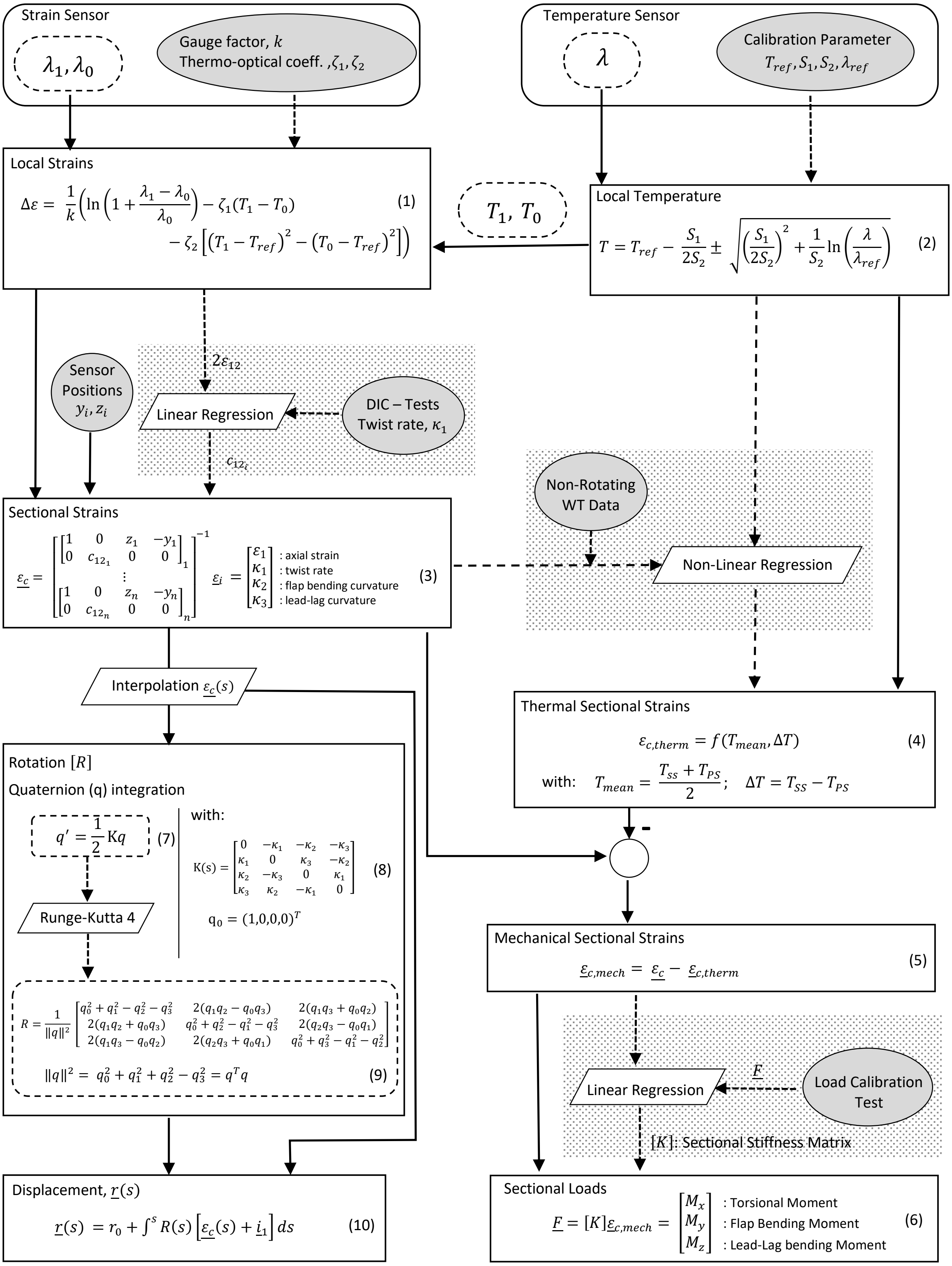

Figure 2. Flowchart

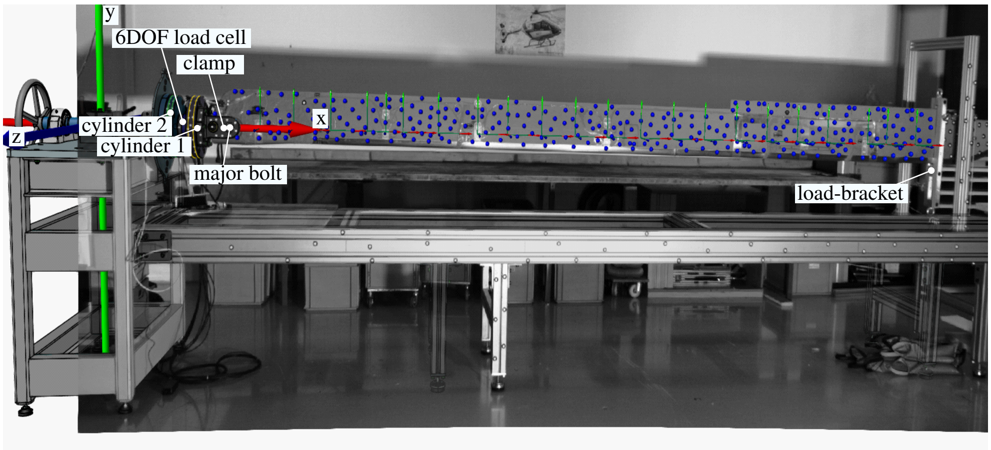

(a) Experimental setup for deformation measurements with superimposed CAD definition

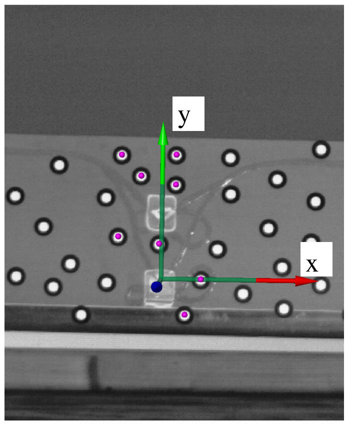

(b) Point component linked to the local coordinate system

Figure 3.

time. A static test with a combined load in all directions was also conducted.

Data was recorded simultaneously by the FBG interrogator for the attached FBG sensors, and by a separate data acquisition unit for the 6-DOF load cell and the 15 electrical resistance strain gauge full bridges. The DIC system recorded eleven *stages* of each load case and test.

A stage is defined as the momentary capture of the combined set of stereo images. After the recording, all stages were further processed with the DIC software *GOM Correlate Professional 2022*. The cylindrical flanges and the plane surfaces of the blade clamp were used for the initial alignment of the measurement data with respect to a coordinate system. The CAD description of the experimental setup was superimposed to the undeformed reference state to align the coordinate system (in blade reference coordinates) to the original target data.

The measured deformation field was split into multiple radial sections. In order to recover the deformed local coordinate system of each section, the neighboring markers were connected to a point component as shown in Figure 3b. The point component links the coordinate system at the beam axis with a rigid body motion. Note that this local sectional coordinate system coincides with the local coordinate system of the deformed beam. For each stage the position vector of the origin and the unit vectors of the local coordinate system were exported for further evaluation.

KINEMATIC STRAIN-DISPLACEMENT RELATION

The objective of this chapter is to derive for each instrumented section a relationship between measured strain signals and beam sectional strains at sensor location i. The sectional strain vector is described as $\varepsilon_c^T = (\bar{\varepsilon}_1, \kappa_1, \kappa_2, \kappa_3)$, with the sectional axial strain $\bar{\varepsilon}_1$, the twisting rate κ_1, the flap bending curvatures κ_2 and the lead-lag bending curvature κ_3.

Equation (3) describes the axial strain field based on Euler-Bernoulli assumptions, which have been proven to be adequate for isotropic homogeneous beams featuring extension and bending. For each sensor i the axial entries of the matrix are defined by the y and z coordinates of the strain sensor. However, the Euler-Bernoulli assumptions provide a poor representation of beams under torsion and are only valid for isotropic cylindrical cross-sections. In general, if the beam is twisted, the cross-section warps and cannot remain plane. For this reason, Saint Venant relaxed the Euler-Bernoulli assumptions (Ref. 15) and introduced a new assumption, stating that after deformation the cross-section warps proportionally to the rate of twist. According to Saint Venant's theory, the axial displacement field is proportional to the twist rate κ_1 and has an arbitrary variation over the cross-section described by the unknown warping function $\Psi_1(y,z)$. The associated strain field can be evaluated based on the strain-displacement relationship to find the strain/twist-rate coefficient c_{12}, which depends on the partial derivatives of the unknown warping function, the sensor location (y,z) and the ply/surface angle θ_1:

$$c_{12} = \left(\frac{\partial \Psi_1}{\partial z} + y\right)\sin(\theta_1) + \left(\frac{\partial \Psi_1}{\partial y} - z\right)\cos(\theta_1) \qquad (11)$$

The previously described optical deformation measurements were used to calibrate the c_{12} coefficients for each shear strain sensor location. First, the twist rate κ_1 was derived from the DIC measurements and correlated to the strain measurements. As explained, grouping optical markers together to form a point component linked the motion of the local coordinate system to that of the group of points. In order to derive the local sectional strains, the spatial derivative was calculated for the derived local coordinate system rotation matrix R with the following equations:

$$\varepsilon_c = \begin{Bmatrix} \underline{\bar{\varepsilon}} \\ \underline{\kappa} \end{Bmatrix} = \begin{Bmatrix} R^T \underline{\bar{r}}' - \underline{\bar{\imath}} \\ \mathbf{axial}(R^T R') \end{Bmatrix} \qquad (12)$$

The axial vector, associated with a second-order tensor A, is

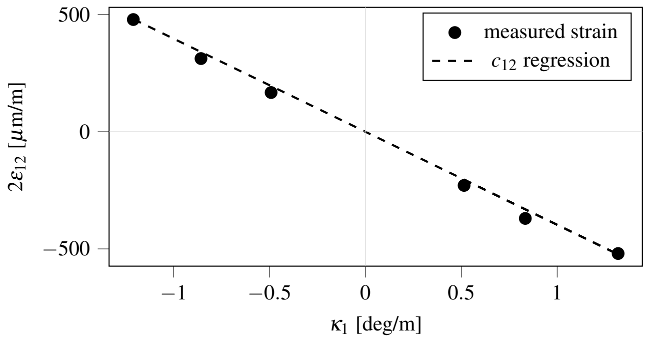

Figure 4. Shear strain (sensors 1-10/1-12) vs. twist rate κ_1

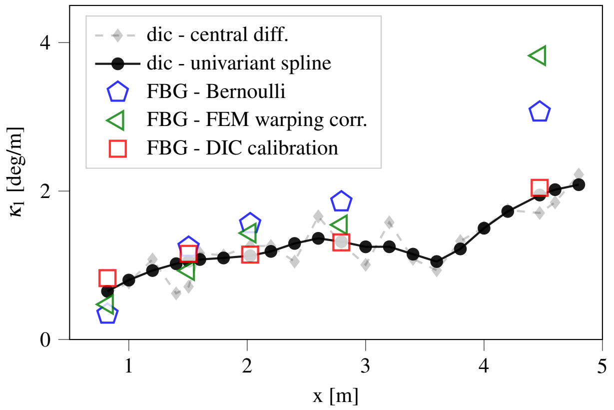

Figure 5. Strain-based twist rate calculation vs. DIC measurements under positive torsional moment

defined as

$$\textbf{axial}\,(A) = \frac{1}{2}\begin{Bmatrix} a_{32} - a_{23} \\ a_{13} - a_{31} \\ a_{21} - a_{12} \end{Bmatrix}. \tag{13}$$

The low out-of-plane accuracy (around 0.3 to 0.5 mm) of the data created significant fluctuations when directly calculating the derivative of the sectional strains obtained from DIC. To address this issue, spline interpolation was employed as a method to smooth the data.

All torsional load measurement cases were used for a linear regression. From the calculated least squares solution the relationship between twist rate and local shear strains could be derived. Figure 4 shows exemplary the shear strain of the sensor pair 1-10/1-12 versus the twist rate κ_1. The dashed line represents the corresponding least squares solution for the coefficient c_{12}.

In order to validate the derived kinematic shear strain relation, the twist rate κ_1 was determined from DIC measurements and compared to the predicted twist rates, as presented in Figure 5. In addition to the approach of the DIC-calibrated c_{12} coefficients, the figure also shows the solution of the Bernoulli representation without warping terms.

According to a further methodology applied for this comparison, the unknown warping displacement was evaluated with the help of sectional finite element models of *SONATA* and the solver *ANBA4*. This hybrid approach was first introduced by Sinotte and Bauchau (Refs. 16–18) and later adopted by Pflumm (Ref. 19).

After interpolating the calculated warping field under unit loads to the FBG sensor location i, as shown in Figure 6, Equation (3) can be rewritten as the sum of the rigid section Euler-Bernoulli model U_i and the unknown warping correction $V_i K$:

$$\varepsilon_i = (U_i + V_i K)\,\varepsilon_c \tag{14}$$

The warping correction term contains the differential operators A and B, the sectional stiffness matrix K, the non-dimensional curvature tensor $\tilde{\mathcal{K}}$, the warping displacement under unit load W and the strain rotation matrix $R_e(\theta_1)$, which ensures a common orientation of all measured strains. The derivation was described by Han and Bauchau (Refs. 20, 21).

$$V_i = R_{e,i}^{-1}\,(AW_iK + BW_i) \tag{15}$$

It was recognized that the warping correction improved the solution at the first four instrumented sections compared to the classical Euler-Bernoulli beam model, yet showed a large offset at the last section. As an educated guess there was a significant discrepancy between the model and the reality, and the influence of the trim tab was not well represented in the model. Said discrepancy revealed the weakness of this inherently implicit hybrid approach. Since the warping corrections were determined from a numerical model, the model itself had to represent the problem accurately.

Figure 5 also shows that the classical Euler-Bernoulli assumptions fail most notably in the last section and that the DIC calibration of the c_{12} coefficient has the smallest overall error. It was therefore the method selected for further analysis.

According to Equataion (6), the symmetric sectional stiffness matrix K establishes a relationship between the sectional strains ε_c and the stress resultant vector F. All datapoints of the measurements create an over-determined system of linear equations that is solved to determine the desired coefficients. For that, the constitutive equation is rewritten in the general form $Ax = b$ by vectorising the sectional stiffness matrix and unraveling the sectional strains. To enforce the symmetry of the sectional stiffness matrix the duplication matrix $D_n \text{vech}(K) = \text{vec}(K)$ is used to unravel the sectional strains $(I \otimes \varepsilon_c) D_n$. The SOE is solved by minimizing the Euclidean 2-norm.

OUTLIER DETECTION

The objective of this chapter is the identification of potential sensor errors or malfunctions by taking advantage of the overdetermination of the instrumented sections. In more detail, the sensor layout per section provided more strain sensors than required to solve the kinematic strain-displacement relationship. This property was used to detect faulty signals, mask them as outliers and exclude them from the further computation.

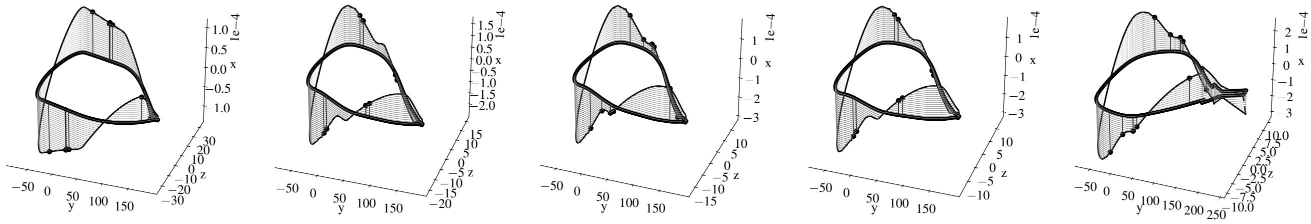

Figure 6. Out-of-plane surface warping field under unit load torsion ($M_x = 1$ Nm), from section R820 to R4470 (left to right)

In the kinematic strain-displacement calculation the problem has been separated into an axial and a shear strain field with two separate linear systems of equations in the form $Ax = b$. The coefficient matrix A_1 contains only the axial sensor positions. In contrast, the coefficient matrix A_2 is an equivalent shear problem, which contains the DIC-calibrated coefficient c_{12} relating the shear strain at sensor position i to the associated twist rate. Thereby transversal shear strains are assumed to be negligible. Both coefficient matrices are a fix property of the instrumented section and do not alter with a varying signal.

$$[\varepsilon_{11}]_i = A_{1,i} \begin{Bmatrix} \varepsilon_1 \\ \kappa_2 \\ \kappa_3 \end{Bmatrix} \tag{16}$$

$$[\varepsilon_{12}]_i = A_{2,i} \left\{ \kappa_1 \right\} \tag{17}$$

For every possible sensor combination up to $M - N$ (number of unknowns $-$ number of sensors), the *Moore-Penrose-Pseudo Inverse* A_1^+ and A_2^+ was calculated, with which the sectional strains and the remaining residuals $|b - Ax|$ could be evaluated from measurement signals.

The sensor combinations and their remaining residuals were compared iteratively to a fixed residual threshold, beginning with a combination of all sensors. If the residual for a combination was higher than the threshold, subsequently an iteration was done over all combinations with one sensor excluded. Then their residuals were compared against the threshold. If one or more combinations meeting the criteria were found, the case with the lowest residual was selected and the sensor outlier was identified. This procedure was continued until the number of sensors was equal to the number of unknowns, which would naturally produce a residual of zero.

The residual, defined by the root mean square error (RMSE), for a load calibration measurement is plotted in Figure 7. The x-axis represents the sample number, the y-axis the RMSE in log scale. The test started from a preloaded condition, upon which the load was released. For high torsional loads, residuals with an order of magnitude three times higher than usual were detected. As the load was further released, their value suddenly dropped towards that of normal residuals. By applying the above methodology, the shear sensor combination *1-10/1-12* was identified as outlier that caused the large discrepancy. Once this sensor was removed from the calculation, the error decreased into normal regions. Since this malfunction only appeared under very high loads that are uncommon during regular operation, it was assumed that the wavelength peak of one of the sensors started to interfere with another peak, neighbored in the optical spectrum of the fiber. Such phenomena is illustrated in the example of Figure 8.

The described approach is an easy and effective method to check for signal consistency in an overdetermined system of equations. It proved to be a fast algorithm for a low number of outliers and small problems with a lot of executions.

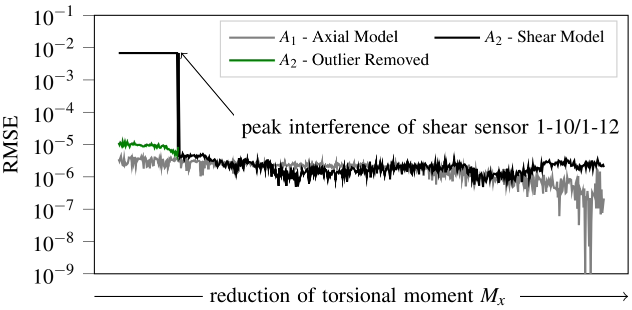

Figure 7. Residuals (RMSE) of the kinematic strain-displacement relationship during the release of high torsional loads

STRAIN-BASED SHAPE RECONSTRUCTION

In this chapter a displacement theory is developed and validated with the objective of providing shape predictions based on strain measurements of the rotor blade during flight. The two common approaches are an integration along the span-wise coordinate of a beam, and a modal shape sensing method. The latter requires the determination of the modal shape functions of the rotor blade during the different operational states and was not considered in the scope of the investigation.

Quaternions are an extension of the complex numbers to form a non-commutative algebra in four dimensions. They provide

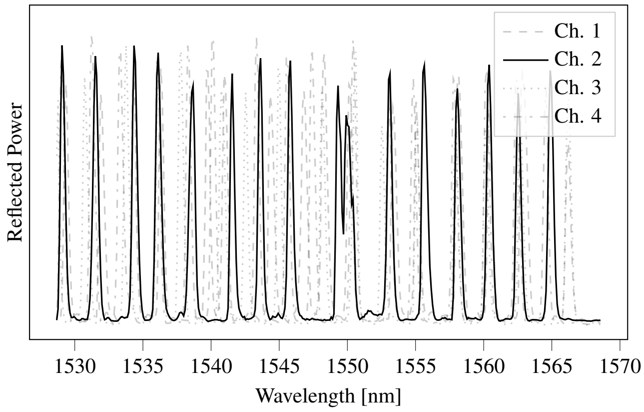

Figure 8. Interference of FBG sensors 2-9 and 2-10 at section R2975 under large static flap bending loads.

a convenient mathematical notation for representing spatial orientation and rotation of elements in the three-dimensional space. More specific, they encode information of an axis-angle rotation about an arbitrary axis. For this purpose, quaternions are treated here as vectors:

$$q = q_0 + q_1 i + q_2 j + q_3 k \quad (18)$$
$$= [q_0 \quad q_1 \quad q_2 \quad q_3]^T \quad (19)$$

As noted in Equation (7), the spatial derivative of a unit quaternion q' is determined by the bending curvatures κ_2 and κ_3, and the twist rate κ_1 within $\mathcal{K}$ of Equation (8) and the quaternion q itself (Ref. 22).

The sectional strains were derived for each instrumented section from the kinematic strain-displacement relationship. Values between data points were estimated by quadratic polynomial interpolation. The initial value problem of a system of ordinary differential equations is numerically integrated with the *Explicit Runge-Kutta* method of order 5(4).

With the transformation of Equation (9) the displacements $r(s)$ are integrated along the span s according to Equation (10).

Figure 9 illustrates the displacements in the flap (z) and chord-wise (y) directions, as well as the twist angle expressed as an Euler angle (X) (θ), for three distinct loads applied using the strain-based shape reconstruction methodology. These results are presented in comparison to the recorded displacements from the DIC measurements. In the case of the chord-wise lead load, the largest displacement in the y-direction was observed, with a tip displacement of -26 mm. The strain-based reconstructed displacements demonstrate an excellent degree of agreement in comparison to the DIC displacements.
Figure 10 illustrates the box plot of the absolute tip displacement error across all recorded load cases, demonstrating a maximum deviation of only 2.6 mm in the y-direction. In the z-direction, the measured tip displacement reached values of up to 74 mm during a flap load case. While the agreement remains satisfactory, the deviation increased to a median of 3.0 mm and a maximum value of 8.1 mm in all load cases. The discrepancy between the reconstructed displacements and the DIC measurements also remains small in the direction of torsion. However, with a maximum deviation of 0.51° at the blade tip, it is still significant, depending on the purpose of application.

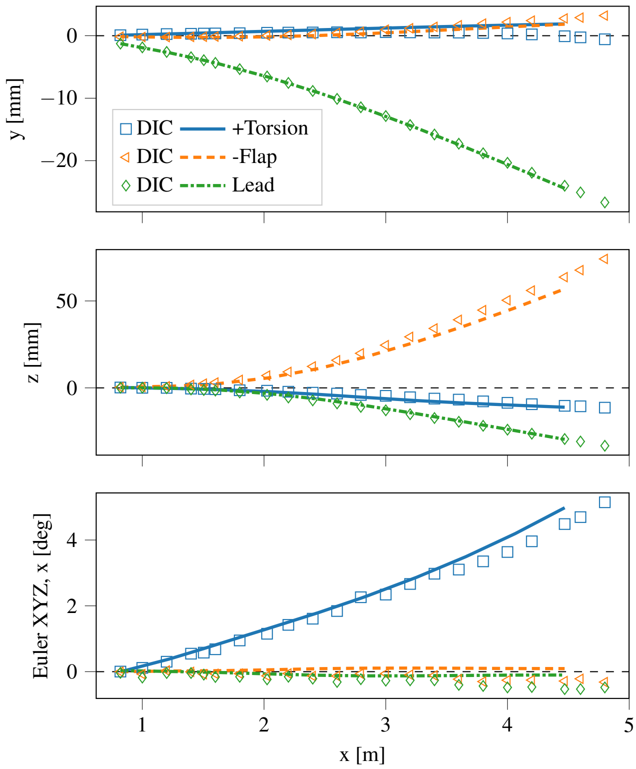

Figure 9. Shape reconstruction vs. DIC measurements

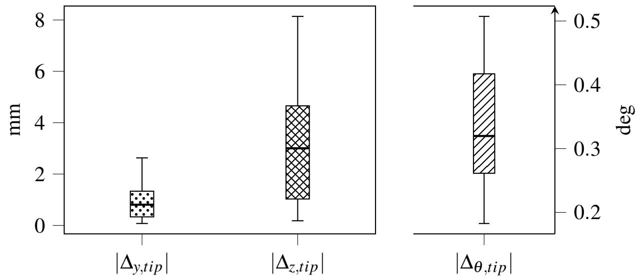

Figure 10. Box plot of the tip displacement error over all static load cases.

The results are noteworthy for all load cases, particularly given the limited number of instrumented sections utilized for support points in the interpolation and integration processes. It is anticipated that further enhancements will be observed with an increase in the number of instrumented sections. It is important to note that the load case does not accurately represent the actual operating conditions. In this test setup, the load was consistently applied as a single load or moment at the tip, which resulted in a linear bending moment distribution along the span and a constant torsional moment. This could result in less favorable outcomes than those observed in the lab tests.

TEMPERATURE COMPENSATION

For the development and demonstration of the thermal calibration model, data of the instrumented blade recorded during a full-scale rotor test rig campaign was taken as basis. In Ref. 23 the setup and program of the campaign is described, which comprised twelve test runs with different configuration and control inputs. All recorded data points contained the temperature information from the two FBG temperature sensors on the two blade surfaces. This chapter investigates the question, whether and to which extent this information can be exploited to improve the accuracy of load measurements by isolating thermal sectional strains.

A preliminary examination of the recorded temperature data – the local temperatures had been determined beforehand with Equation (2) – revealed an obvious influence of the dynamic blade state on the temperature recordings. Figure 11 suggests a dependency of the temperature signals from the rotational speed, which resulted from the airflow conditions. However, it also shows a timely lag of said dependency, indicating heat transfer processes within the blade structure and between the blade and its environment. Since airflow conditions varied significantly both span-wise and chord-wise along the blade during rotation, the data available from two temperature sensors did not suffice for a quantitative analysis.

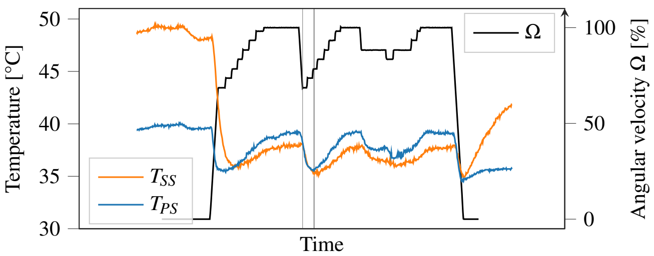

Figure 11. Control inputs and temperature sensor signals for a rotational speed sweep test run. The vertical lines indicate local minima of the temperature recordings and rotational speed.

Figure 11 also contains two time periods in non-rotating condition, one before and one after the test run. While the temperature signals in the first period show a balanced state with a remarkable temperature difference between the sensors, the second period is characterized by initially even temperatures followed by an increase of the suction side temperature. Thus, the recorded temperature data contains both a spatial and a temporal gradient.

As illustrated in Figure 12, the sectional strains did not remain stable during the second period, contrary to what would be expected in a non-rotating condition with constant mechanical loads. Instead, a correlation with temperature influences is indicated. As Equation (2) already accounted for the thermo-optic effect, the observed behavior could be explained by the effect of thermal sectional strains, represented by the parameter $\varepsilon_{c,therm}$.

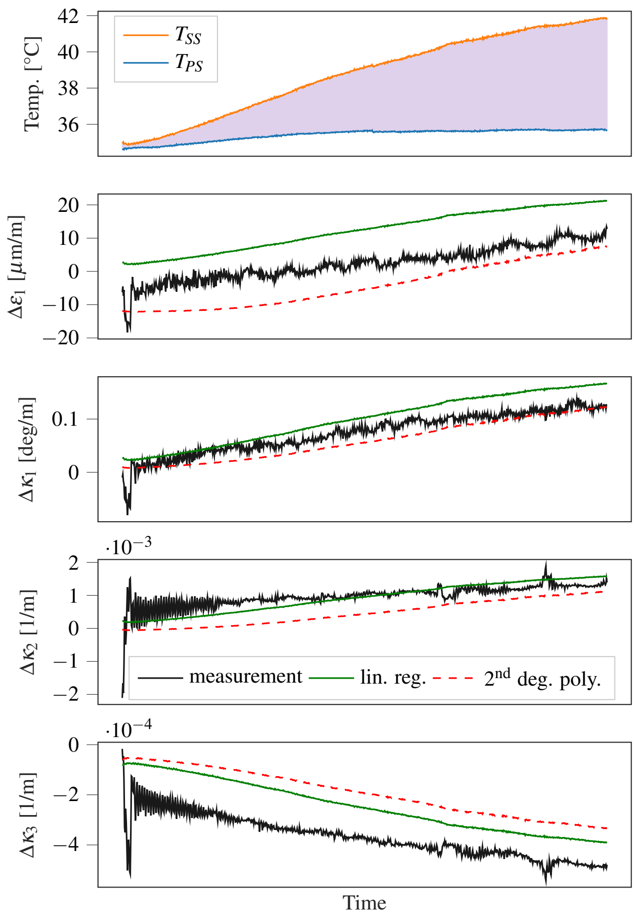

Figure 12. Values derived from the two temperature sensors and sectional strains determined for section R820 during a period directly after stopping the whirl tower rotation

Particularly interesting to the development of a relationship between cross-sectional strains and thermal influences were the FBG recordings before and after rotation. On the one hand, the mechanical loads were repeatable and approximately constant during these periods, since there were barely wind or gusts and the rotor controls were in a defined state. On the other hand, the temperature range measured on the blade was comparably broad. This was due to changing sun elevation, shade and ambient temperature over the course of the test campaign, but also a useful side effect of the thermal imbalance right after stopping the rotor spinning. 23 such time snippets could be extracted from the recorded data as illustrated in Figure 13. Each of them could be allocated to one of three different general temperature characteristics: the two states described above (*balanced*, *increase*), as well as a state of decreasing temperatures (*decrease*). The weather conditions during the testing period had been sunny and dry, mostly free of wind or gusts, and the ambient temperature had varied in a range from 21°C to 30°C. The temperature state *increase* usually arised, when the instrumented blade after rotation had stopped in a rest position exposed to the sun. Consequently the temperature on the suction side had increased significantly faster than on the pressure side. On the other hand, a blade rest position in the shade of surrounding trees, which had occurred in the late afternoon, lead to a *decrease* state.

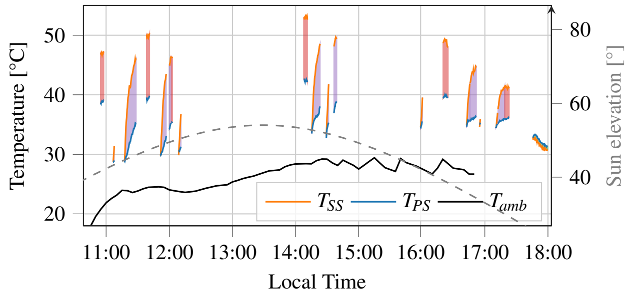

Figure 13. Selected time periods in non-rotating condition with temperature sensor recordings, ambient temperature and sun elevation

It was seen as desirable to quantify the thermal sectional strains and subtract them from the sectional strains, in order to yield the pure mechanical sectional strains according to Equation (5). With available temperature data only from two sensors the prospects of such a regression task appeared to be limited, however worth to be investigated. Ideally this would lead to a model that can be applied in arbitrary conditions, i.e. also for the determination of mechanical sectional strains during rotation.

The used data set was composed of the 23 time periods in non-rotating condition, taken as discrete data points. Three of the time periods – one of each state *balanced*, *increase* and *decrease* – were put aside as test set. The performance of the investigated regression models was measured using the root mean square error (RMSE).

In order to facilitate interpretation, a local reference state was selected within the measurement data, for which the thermal component of the sectional strain was set to zero. The reference point was taken at the end of the last time period, because due to the blade stop position in the shade not only the temperatures, but also their timely and spatial gradients were low.

The model $\varepsilon_{c,therm} = f(T_{mean}, \Delta T)$, as noted in Equation (4), was trained with twenty labels, representing the four-value sectional strain vector at five blade sections. The feature vector comprised two values, which were the mean temperature of the two sensors, as well as the difference of the temperature values. The latter represents the spatial gradient between the two sensor locations.

Figure 14 shows the RMSE for a linear regression analysis and a 2nd degree polynomial analysis on the training set, a 5-fold cross-validation (development) set with standard deviation error bar, and on the test set. Despite the limited bandwidth of the data set, predominantly linear correlations were observed, and an increase of the model order resulted in a reduction of the error measure for both the training and development sets. However, this did not translate to satisfactory generalization for the selected cases in the test set. To illustrate the effects and enhance interpretability, a simple linear regression model was employed for the following analysis.

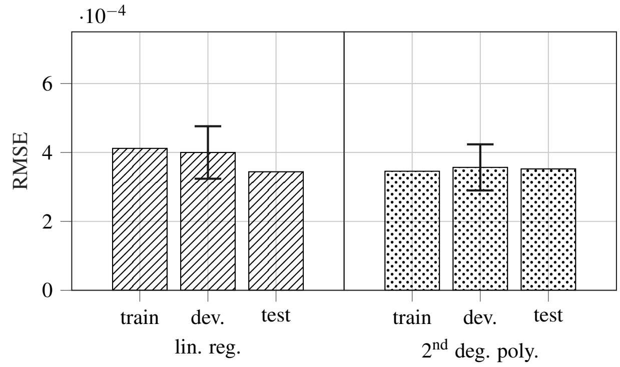

Figure 14. Model performance comparison

Figure 12 shows exemplarily the target and predicted values for the sectional strains at blade section R820 for a test set time series in *increase* state. The overall trend of both models aligns closely with the observed data, although a discernible offset is evident in subsets of the test set.

Figure 15 illustrates the deformation of the rotor blade due to a mean temperature increase of +15°C and a temperature difference between the suction side and the pressure side of +5°C and +10°C, respectively. This was achieved using the strain-based shape reconstruction method, which is presented in this study, and which was compared to the reference state. An average temperature increase of 15°C resulted in a bending of the rotor blade of approximately 6.5 mm in a backward direction and 6.8 mm in an upward direction at the blade tip. In contrast, a positive temperature difference lead to a blade deformation in the opposite direction. Additionally, the temperature increase caused a notable twist of the rotor blade. Regarding the deformation reconstruction results presented above, it is essential to exercise caution when interpreting the absolute values, as they merely illustrate a trend. Regrettably, these deformation measurements could not be compared to a second instance such as DIC measurements.

Figure 16 illustrates the impact of the three exemplary temperature states on the *phantom sectional loads*, which are defined as the thermal sectional strains multiplied by the sectional stiffness matrix, denoted as $F_{ph} = K\varepsilon_{c,therm}$. These phantom loads are quantities which would have been registered incorrectly, if this type of temperature compensation had not been carried out.

For example in absolute terms, a phantom torsional moment of 42 Nm would have been observed at the first instrumented section when a temperature differential of +10°C was present.

To summarize, a thermal compensation methodology has been presented, which allows to isolate the thermal influences on the sectional strain values by the recorded temperature signals and therefore improve the accuracy of load measurements in varying environmental conditions. The temperature recordings gave insights into the temperature condition on the blade

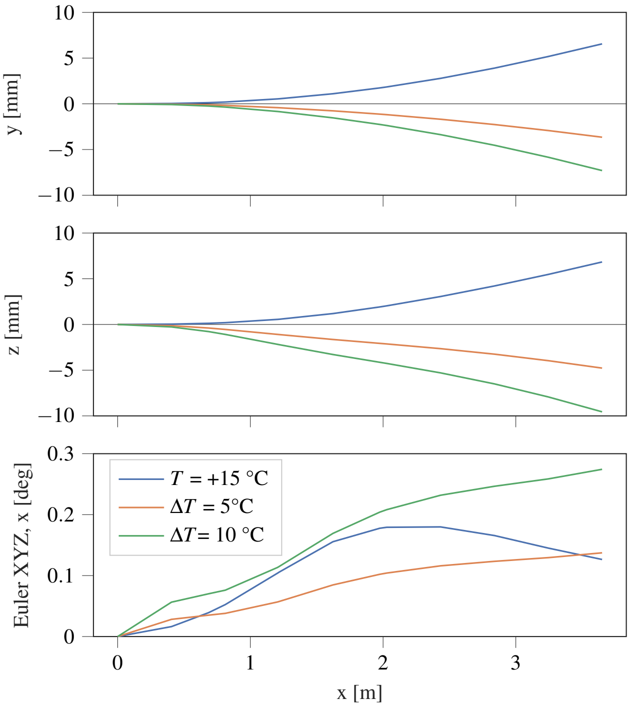

Figure 15. The effect of temperature on the elastic deformation of the rotor blade. Derived with the described shape reconstruction methodology.

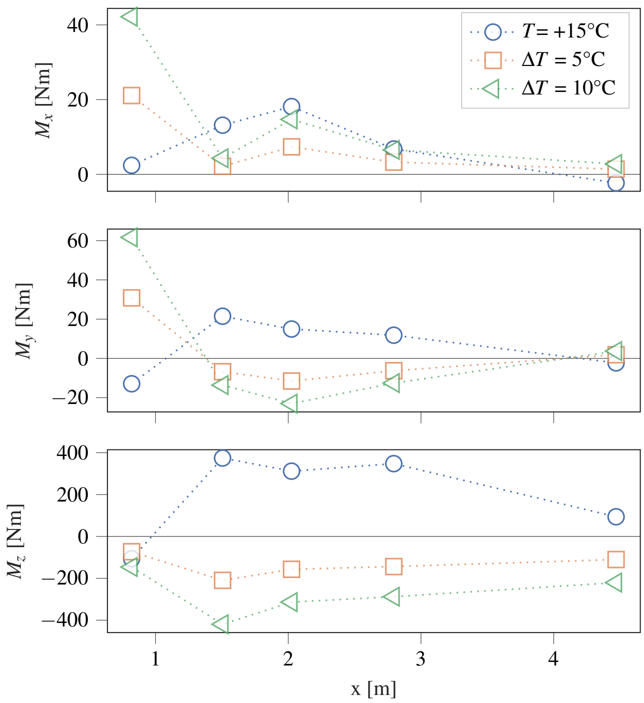

Figure 16. Phantom sectional loads of the rotor blade due to temperature effects.

surface both in rotating and non-rotating state. Furthermore, the limitations of this study have been outlined, primarily resulting from the number and location of temperature sensors and limited data set.

Improved data quality and sensor placement are key to enhancing the accuracy of the regression model. To achieve this, future studies should particularly expand the data set and optimize the distribution of temperature sensors. Embedding sensors into the structure could further minimize external influences. The presented method is not exclusive to FBG-instrumented rotor blades; it can also be applied to classical strain-gauge instrumented beams in general.

Furthermore, the presented method is intended as an in-field procedure, avoiding the necessity for supplementary laboratory tests for thermal recalibration. This results in a reduction of the overall effort and costs associated with the instrumented component. In this procedure, the aircraft equipped with instrumented blades gathers strain and temperature data on a regular basis, whenever mechanical conditions remain constant. Once a sufficient quantity of data has been accumulated, the regression model is determined and evaluated against former parameters. This also paves the way for further monitoring capabilities and the potential to identify degraded sensors or structural damage.

CONCLUSIONS

The implementation of load monitoring systems has the potential to enhance aviation safety and reduce maintenance costs. However, the current limitations of sensor technology, particularly in terms of size, weight and reliability, are hindering the widespread adoption of these systems on the rotor.

In this study, a pre-series Kopter AW09 main rotor blade was instrumented with fiber Bragg gratings (FBGs). Static lab tests with digital image correlation (DIC) were conducted to derive and evaluate mathematical relationships between the measured strain signals and structural quantities. These comprised the beam sectional strains, the elastic deformation of the blade, and the sectional loads and stiffness properties. Furthermore, the paper addressed the challenge of isolating these target variables from the influence of temperature variations.

The following key conclusions were drawn from this study:

1. A linear relationship between the shear strain at sensor position i and the twist rate κ_1 was identified with the use of DIC. The primary advantage is that it is entirely based on experimental data, avoiding the necessity of complex finite element models. Furthermore, it represents a crucial advancement compared to the inaccurate Euler-Bernoulli relationship.
2. An outlier detection method was presented which improved the robustness of the measurement system against sensor failures by exploiting the over-determination of each instrumented section. In the case of spectral peak interference, erroneous signals could effectively be removed from the data set. This demonstrated a key advantage over current strain gauge instrumentation in terms of reliability and potential suitability for load-monitoring applications.
3. A novel strain-based shape reconstruction method was developed and validated, which considers axial, bending

and twist deformation of the rotor blade without relying on predetermined mode shapes. The method demonstrated notable accuracy in comparison to the reference deformation captured by the DIC system.

4. A methodology for the experimental determination of rotor blade sectional stiffness properties was developed, with the primary intention of establishing the relation between sectional strains and sectional loads. Additionally, the methodology can be used to validate the structural numerical models of the rotor blade and the beam descriptions of aeromechanic models. Furthermore, the methodology has the potential to be employed for quality assurance purposes in production, thereby reducing the uncertainties associated with stiffness properties, and improving rotor track and balance behavior.

5. A thermal compensation methodology was presented, which effectively isolated thermal effects on sectional strain measurements. Under consideration of the anisotropic behavior of the structure and non-uniform temperature distributions, load accuracy under varying environmental conditions was enhanced. Temperature data provided valuable insights into blade surface conditions. While the current study was limited by the quantity and placement of the sensors and the data set size, the proposed method showed potential for improvement with data expansion and an optimized sensor distribution. The technique is applicable beyond FBG-instrumented rotor blades and offers the advantage of in-field implementation, reducing costs and effort. In future work the potential of the method for structural health monitoring can be explored.

ACKNOWLEDGMENTS

This work was supported by the Bavarian ministry of economic affairs, regional development and energy (StMWi) through the Bavarian research program BayLu25 in the project iRoB.
The authors would like to thank the Kopter component testing department for their incredible support during the project, in particular Slawomir Wybranski, Michael Gallo, Max Volk, Max Hönig, Giuseppe Bonanno, Marc di Guisto, Pietro Zugnoni, Luciano Saraiello, Federico Savorgnan, Safoura Bazrafshan, Venkatrao Mallipudi and Tim Niggemann.
We also gratefully acknowledge Florian Berghammer for his assistance in preparing the FBG instrumentation, and Collins Aerospace, especially Pete Carini and colleagues, for their support with the Aeromini interrogator.

Supported by

Bavarian Ministry of Economic Affairs,
Regional Development and Energy

AUTHOR CONTACT INFORMATION

Tobias Pflumm: tobias.pflumm@koptergroup.de
Andreas Jochum: andreas.jochum@koptergroup.de
Sören Süße: soeren.suesse@koptergroup.de

REFERENCES

1. Isom, J. D., Davis, M. W., Cycon, J. P., Rozak, J. N., and Fletcher, J. W., "Flight Test of Technology for Virtual Monitoring of Loads," American Helicopter Society 69th Annual Forum, 2013.

2. Hajek, M., Manner, S., and Suesse, S., "Blade Root Integrated Optical Fiber Bragg Grating Sensors – A Highly Redundant Data Source For Future HUMS," *American Helicopter Society 71st Annual Forum*, 2015.

3. Manner, S., *Validierung eines hybriden Sensornetzwerks im Hubschrauberrotorblatt*, Dissertation, Technische Universität München, München, 2016.

4. Suesse, S., and Hajek, M., "Rotor Blade Displacement and Load Estimation with Fiber-Optical Sensors for a Future Health and Usage Monitoring System," American Helicopter Society 74th Annual Forum, 2018.

5. Pflumm, T., Barth, A., Kondak, K., and Hajek, M., "Auslegung und Konstruktion eines Hauptrotorblattes für ein in extremen Flughöhen operierendes Drehflügel-UAV," Deutscher Luft- und Raumfahrtkongress, Rostock, 2015.

6. Bottasso, L. M., Sala, G., Bettini, P., Tagliabue, P., Corbani, F., Platini, E., Guerra, A. B., and Anelli, A., "Rugged Fiber Optics Monitoring System for Helicopter Rotor Blades," 44th European Rotorcraft Forum, Delft, The Netherlands, 2018.

7. James, S. W., Kissinger, T., Weber, S., Mullaney, K., Chehura, E., Pekmezci, H. H., Barrington, J. H., Staines, S. E., Charrett, T. O. H., Lawson, N. J., Lone, M., Atack, R., and Tatam, R. P., "Fibre-optic measurement of strain and shape on a helicopter rotor blade during a ground run: 1. Measurement of strain," *Smart Materials and Structures*, Vol. 31, (7), June 2022, pp. 075014. DOI: 10.1088/1361-665x/ac736d.

8. Weber, S., Kissinger, T., Chehura, E., Staines, S., Barrington, J., Mullaney, K., Fragonara, L. Z., Petrunin, I., James, S., Lone, M., and Tatam, R., "Application of fibre optic sensing systems to measure rotor blade structural dynamics," *Mechanical Systems and Signal Processing*, Vol. 158, September 2021, pp. 107758. DOI: 10.1016/j.ymssp.2021.107758.

9. Kissinger, T., Correia, R., Charrett, T. O. H., James, S. W., and Tatam, R. P., "Fiber Segment Interferometry for Dynamic Strain Measurements," *Journal of Lightwave Technology*, Vol. 34, (19), October 2016, pp. 4620–4626. DOI: 10.1109/jlt.2016.2530940.

10. James, S. W., Kissinger, T., Chehura, E., Mullaney, K., Pekmezci, H. H., Barrington, J. H., Staines, S. E., Tatam, R. P., Lone, M., and Weber, S., "Dynamic and Measurement of Strain and Shape on a Rotating and Helicopter Rotor," Proceedings - ettc2020, 2016. DOI: 10.5162/ettc2020/1.5.

11. Kissinger, T., James, S. W., Weber, S., Mullaney, K., Chehura, E., Pekmezci, H. H., Barrington, J. H., Staines, S. E., Charrett, T. O. H., Lawson, N. J., Lone, M., Atack, R., and Tatam, R. P., "Fibre-optic measurement of strain and shape on a helicopter rotor blade during a ground run: 2. Measurement of shape," Vol. 31, June 2022. DOI: 10.1088/1361-665x/ac736c.

12. Berghammer, F., Heuschneider, V., and Hajek, M., "Development and Integration of a Fiber-Optical Sensor System for Rotor Blade State Observation," Proceedings of the Vertical Flight Society 78th Annual Forum, May 2022. DOI: 10.4050/f-0078-2022-17559.

13. Berghammer, F., Sosa, B., Heuschneider, V., Yavrucuk, I., and Hajek, M., "Testing of a Fiber-Optical Sensor System for Rotor Blade HUMS," Proceedings of the Vertical Flight Society 79th Annual Forum, May 2023. DOI: 10.4050/f-0079-2023-18090.

14. Heuschneider, V., Berghammer, F., Pflumm, T., and Hajek, M., "Development and Initial Hover Testing of the Mach Scaled Rotor Test Rig MERIT," 47th European Rotorcraft Forum, United Kingdom, 2021.

15. Bauchau, O. A., and Craig, J. I., *Structural Analysis - with Applications to Aerospace Structures*, Springer-Verlag GmbH, August 2009.

16. Sinotte, T. M., and Bauchau, O. A., "Novel Approach for Experimental Measurement of Sectional Stiffness Properties of Composite Rotor Blades," 45th European Rotorcraft Forum, Warsaw, Poland, 2019.

17. Sinotte, T. M., and Bauchau, O. A., "Experimental Measurement of Sectional Stiffness Properties of Composite Rotor Blades," Vertical Flight Society 76th Annual Forum, 2020.

18. Sinotte, T. M., *A Strain-Based Experimental Methodology for Measuring Sectional Stiffness Properties of Composite Blades*, Ph.D. thesis, University of Maryland, 2020.

19. Pflumm, T., *Numerical and Experimental Structural Beam Analysis for the Development of Helicopter Rotor Blades*, Dissertation, Technische Universität München, October 2022.

20. Han, S., and Bauchau, O. A., "Nonlinear three-dimensional beam theory for flexible multibody dynamics," *Multibody System Dynamics*, Vol. 34, (3), October 2014, pp. 211–242. DOI: 10.1007/s11044-014-9433-8.

21. Bauchau, O. A., and Han, S., "Three-Dimensional Beam Theory for Flexible Multibody Dynamics," *Journal of Computational and Nonlinear Dynamics*, Vol. 9, (4), July 2014. DOI: 10.1115/1.4025820.

22. Rucker, C., "Integrating Rotations and Using Non-Unit and Quaternions," *IEEE Robotics and Automation Letters*, Vol. 3, (4), October 2018, pp. 2979–2986. DOI: 10.1109/lra.2018.2849557.

23. Pflumm, T., Komp, D., Bilgin, Z., Jochum, A., and Süße, S., "Rotor Component Load Reconstruction for Fiber-Bragg Instrumented Rotor Blades," *50th European Rotorcraft Forum*, 2024.